Design and Quantitative Assessment of Teleoperation-Based Human–Robot Collaboration Method for Robot-Assisted Sonography

Weiyong Si, *Member, IEEE*, Ning Wang, *Member, IEEE*, and Chenguang Yang, *Fellow, IEEE*

***Abstract*— Tele-echography has emerged as a promising and effective solution, leveraging the expertise of sonographers and the autonomy of robots to perform ultrasound scanning for patients residing in remote areas, without the need for in-person visits by the sonographer. Designing effective and natural human-robot interfaces for tele-echography remains challenging, with patient safety being a critical concern. In this article, we develop a teleoperation system for robot-assisted sonography with two different interfaces, a haptic device-based interface and a low-cost 3D Mouse-based interface, which can achieve continuous and intuitive telemanipulation by a leader device with a small workspace. To achieve compliant interaction with patients, we design impedance controllers in Cartesian space to track the desired position and orientation for these two teleoperation interfaces. We also propose comprehensive evaluation metrics of robot-assisted sonography, including subjective and objective evaluation, to evaluate tele-echography interfaces and control performance. We evaluate the ergonomic performance based on the estimated muscle fatigue and the acquired ultrasound image quality. We conduct user studies based on the NASA Task Load Index to evaluate the performance of these two human-robot interfaces. The tracking performance and the quantitative comparison of these two teleoperation interfaces are conducted by the Franka Emika Panda robot. The results and findings provide guidance on human-robot collaboration design and implementation for robot-assisted sonography.**

***Note to Practitioners*—Robot-assisted sonography has demonstrated efficacy in medical diagnosis during clinical trials. However, deploying fully autonomous robots for ultrasound scanning remains challenging due to various constraints in practice, such as patient safety, dynamic tasks, and environmental uncertainties. Semi-autonomous or teleoperation-based robot sonography represents a promising approach for practical deployment. Previous work has produced various expensive teleoperation interfaces but lacks user studies to guide teleoperation interface selection. In this article, we present two typical teleoperation interfaces and implement a continuous and intuitive teleoperation control system. We also propose a comprehensive evaluation metric for assessing their performance. Our findings show that the haptic device outperforms the 3D Mouse, based on operators' feedback and acquired image quality. However, the haptic device requires more learning time and effort in the training stage. Furthermore, the developed teleoperation system offers a solution for shared control and human-robot skill transfer. Our results provide valuable guidance for designing and implementing human-robot interfaces for robot-assisted sonography in practice.**

***Index Terms*— Robot-assisted sonography, continuous and intuitive teleoperation, teleoperation control, human–robot collaboration, human–robot interface.**

Manuscript received 18 October 2023; revised 6 December 2023; accepted 23 December 2023. This article was recommended for publication by Associate Editor H. Su and Editor G. Fortino upon evaluation of the reviewers' comments. *(Corresponding author: Chenguang Yang.)*

This work involved human subjects or animals in its research. Approval of all ethical and experimental procedures and protocols was granted by the Faculty Research Ethics Committee and the UWE Research Ethics Committee under Application No. FET-2122-59.

Weiyong Si is with the Bristol Robotics Laboratory, University of the West of England, BS16 1QY Bristol, U.K., and also with the School of Computer Science and Electronic Engineering, University of Essex, CO4 3SQ Colchester, U.K.

Ning Wang and Chenguang Yang are with the Bristol Robotics Laboratory, University of the West of England, BS16 1QY Bristol, U.K. (e-mail: cyang@ieee.org).

Color versions of one or more figures in this article are available at https://doi.org/10.1109/TASE.2024.3350524.

Digital Object Identifier 10.1109/TASE.2024.3350524

I. Introduction

SONOGRAPHY, also known as ultrasound scanning, is a widely available tool for screening and assessing a variety of pathologies without the use of ionizing radiation. Sonography is often the first line of investigation for assessing solid organs of the abdomen, vessels with blood flow such as the aorta and deep veins of the distal limbs, and small soft tissue structures [1]. With the recent development of collaborative robots, robot-assisted ultrasound scanning has gained significant attention from both the robotics and medical examination communities [2]. This has led to the development of robot-assisted tele-echography systems, which are designed to assist medical experts in acquiring high-quality ultrasound images [3], [4], [5]. There are a number of research works on robot-assisted sonography [6], [7], [8], [9]. In [10], an adaptive ultrasound scanning system was developed for imaging the human spine. In [11], a hierarchical control structure, including force control and orientation control, was developed for teleoperation-based ultrasound scanning. The latest review paper summarised the progress of robotic sonography [12], [13]. Fully autonomous ultrasound scanning by robots is challenging to deploy in practice due to uncertain tasks, patient safety, and the need for dexterous manipulation, such as orientation, motion, and force regulation. Tele-echography has emerged as a promising and effective solution, combining sonographers' expertise with robots' autonomy to perform

ultrasound scanning for patients residing in remote areas. This approach eliminates the need for in-person visits by the sonographer, enabling high-quality medical care to be delivered remotely.

Teleoperation is a well-established research area that has been the subject of numerous theoretical and experimental studies since the 1950s [14]. This approach has proven particularly effective in controlling robotic manipulators performing complex tasks that require dexterous manipulation and high-level intelligence. For example, the authors propose a novel tele-manipulation scheme that enables both the individual and combined control of any number of robotic arms [14]. The combination of human intelligence and experience with robot autonomy makes teleoperation an effective approach for performing a variety of dexterous tasks, including medical examination and robot-assisted healthcare, etc. However, most of the work focuses on tracking control, communication delay and data loss, transparency and stability of the teleoperation system. Human-robot interaction and collaboration through teleoperation, such as robot-assisted telediagnostics and telemedicine, have attained increasing attention, and a number of research efforts related to these topics have been investigated, especially since the COVID-19 pandemic [9], [15]. For example, a range of human-robot collaboration interfaces through teleoperation[1] and shared control frameworks are developed to achieve human-robot collaboration tasks. Because human-robot collaboration provides an effective approach to combining human intelligence and the autonomy of robots, it could improve the safety and efficiency of the robot performing dexterous manipulation tasks. In addition, the intuitive and natural human-robot interface is vital for robot skill learning, such as learning from human demonstration [16], human-in-the-loop robot skill learning, and interactive learning [15] etc. More recently, brain-inspired or human-inspired methods have been proposed to design intelligent robotic systems from the behaviour and neural-inspired aspect [17], [18]. Multiobjective optimization and advanced control algorithms are investigated to improve the control performance of the precise assembly [19], [20], [21], [22]. However, developing an intuitive and immersive human-robot interface with multimodal feedback for human-robot interaction and collaboration is still essential and challenging.

So far, a number of teleoperation interfaces have been developed [24], as shown in Fig.1. A detailed comparison of various teleoperation interfaces is presented in Table I. The intuitive and natural interface is significantly essential for human-robot interaction and even human-robot skill transfer, especially for dexterous manipulation tasks, such as medical examination [3]. These days multimodal feedback-based teleoperation systems are studied, e.g., visual feedback, haptic feedback and audio feedback, to help human operators sense remote scenarios. However, various teleoperation interfaces make it difficult for system designers to select a suitable teleoperation interface for their tasks. Although the [29] studies the quantitative physical ergonomics assessment for teleoperation interface, the task is an assembly task that is different from the ultrasound scanning. There is a research gap in comprehensive metrics for robot-assisted medical examination.

[1]Human-robot interaction and collaboration interface refer to human-robot collaboration through teleoperation in this article.

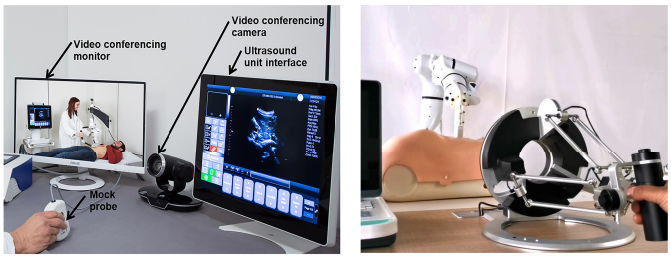

(a) (b)

Fig. 1. Two typical teleoperation interfaces for robot-assisted tele-sonography. (a) is a probe-like teleoperation device without haptic feedback. (b) is a customised teleoperation interface with haptic feedback.

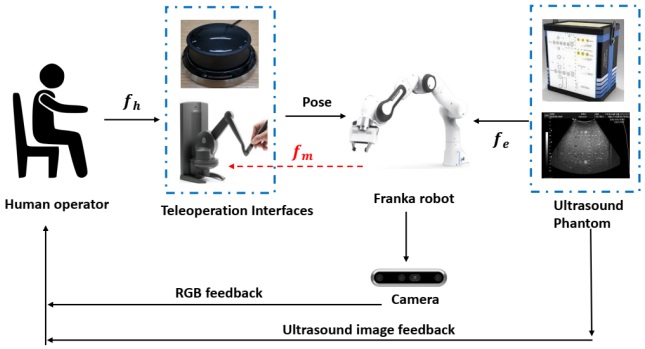

Fig. 2. The teleoperation system structure.

The teleoperation interface is significantly important for human-robot interaction and human-robot skill transfer [30]. Multimodal feedback, e.g., visual feedback, haptic feedback and audio feedback, may help human operators improve scenario awareness. In this work, one of the contributions is the user study for tele-sonography interface, and the results can be used to guide the design of teleoperation interfaces for medical examination. The conclusion and finding can also be employed in the human-robot skill transfer and learning from human demonstration or interaction, and human-in-the-loop mechanism. The main contributions of this paper can be summarized as follows:

- We develop a teleoperation system for robot-assisted sonography with two different interfaces, a haptic device-based interface and a low-cost 3D Mouse-based interface, which can achieve continuous and intuitive telemanipulation by a leader device with a small workspace, compared with [23], [24], and [28]. We evaluate these two teleoperation interfaces, and guidance on designing teleoperation interface for tele-sonography is provided.
- We also propose comprehensive evaluation metrics of robot-assisted sonography, including subjective and objective evaluation, to evaluate tele-echography interfaces and control performance. We study the ergonomic performance based on the estimated muscle fatigue and compare the quality of the acquired ultrasound images. To evaluate the proposed method, we conducted user

TABLE I
COMPARISON OF DIFFERENT TELEOPERATION INTERFACES

A taxonomy of human-robot interfaces	Hardware devices	Literature	Advantages	Disadvantages
Augmented Reality	Depth cameras and monitors; Head-mounted display (HMD).	[23] [24]	Visual feedback; Virtual feedback; Authenticity and synchronization.	Time delay; Non-intuitive teleoperation.
Robot interface	A robotic arm with same configuration as the follower robot.	[25]	Intuitive teleoperation; Tactile and audiovisual feedback	Two robot arms with the same configuration are needed.
Haptic interface	Omni Touch joystick; Omega; Wearable haptic device.	[11] [3] [26] [27] [28]	Haptic feedback; Combining kinesthetic, vibrotactile and visual feedback.	Time delay; Complex and expensive

studies involving six participants using the robot-assisted sonography standard Phantom.

The remaining of the paper is as follows: Section II presents the related work, including ultrasound image quality and ergonomic assessment of the teleoperation interface. The preliminary knowledge and methods are presented in Section III. In IV, we present the design and evaluation metrics of the teleoperation system. The design of the experiment and the results and performance analysis are presented in Section V. Finally, conclusions and future work are given in Section VI.

II. RELATED WORK

A. Teleoperation-Based Robot-Assisted Sonography

The teleoperation system of robot-assisted sonography has been studied for more than twenty years. For example, in earlier times, the teleoperation system for remote ultrasound scanning has been studied in [31]. In [32], the teleoperation system with haptic feedback was developed for the steerable flexible needles based on the ultrasound image.

Recently, some advanced teleoperation with multiple-modal interface has been studied. In [23], an Augmented reality (AR) teleoperation interface was developed to reduce the time delay in ultrasound scanning. In [33], a multimodal feedback teleoperation system was developed to provide sonographers with a better experience by designing a virtual ultrasound probe on the human side. In addition, some novel control schemes were investigated to improve the teleoperation control system. In our previous work [34], a shared control method was investigated to improve control performance and reduce the workload of human operators for ultrasound scanning.

The robot-assisted teleoperation has been an effective solution method to attain ultrasound images. For example, in [35], a tele-controlled ultrasound scanning system was developed to achieve three-dimensional imaging. The robot-assisted ultrasound scanning system was developed to attain the ultrasound images of human spines [36], [37].

B. Ultrasound Image Quality

One of important metrics is the ultrasound image quality. To evaluate the ultrasound image quality, a common method is scoring the image quality by sonographers. However, this method is time-consuming and expensive, especially for a large number of ultrasound images. Some automatic image quality assessment methods are investigated in the past few years. The confidence map (CM) is used to evaluate the image quality, and the CM can also be used to adjust the probe to the middle of the window [9]. For example, the authors proposed the visual servoing method based on the ultrasound confidence map to optimise the ultrasound image quality [9]. Recently, Jiang et al. developed a vision-based ultrasound system to precisely reposition the robotic ultrasound arm, and a confidence-based optimisation algorithm was investigated to avoid the gap between the probe and contact surface [7]. In addition, the confidence map technique also was used to optimise the orientation of the ultrasound probe to automatic normal positioning [6].

C. Ergonomics Assessment of Teleoperation Interface

Physiological changes can affect the electrical activity of the muscle [38]. Surface Electromyography (sEMG) involves a weighted summation of motor unit action potentials propagating along muscle fibres, making it a useful tool for identifying and detecting muscular fatigue. This non-invasive method of fatigue assessment is an alternative to other methods such as lactate concentration in blood.

Increases in signal amplitude have been observed when detecting muscular fatigue through sEMG, as the body tries to maintain the required level of force. Fatigue has also been strongly linked to changes in the power spectral density (PSD) of sEMG. During maximal contractions, PSD shifts towards lower frequencies, which is generally attributed to a decrease in muscle fiber conduction velocity. Additionally, changes in the number and synchronization of the recruited motor units and the activation of new ones can also play a role in this shift.

III. PRELIMINARIES

A. Redundant Manipulator Dynamics in Cartesian Space

The dynamics of the general serial manipulator robot in joint space can be modelled as,

$$M(q)\ddot{q} + C(q,\dot{q})\dot{q} + G(q) + \tau_f(\dot{q}) + \tau_{\text{ic}} + d_u = \tau_c + \tau_{ext} \tag{1}$$

where the $M(q)$ is the inertia matrix, the $C(q,\dot{q})$ is the Coriolis term and $G(q)$ represents gravitational force. τ_{ic} is the friction torque, $\tau_f(\dot{q})$ is friction torque d_u is the unmodel and uncertainty; τ_c is the control torque. q, $\dot{q}$ and $\ddot{q}$ represent the joint position, velocity and acceleration respectively.

Property 1: Matrix $M(q)$ is symmetric and positive definite.

Property 2: Matrix $\dot{M}(q) - 2C(q,\dot{q})$ is a skew-symmetric matrix.

The relationship between the joint torque and the wrench can be described as,

$$\tau_{ext} = J^T(q) f_e \tag{2}$$

where $J(q)$ is the Jacobian matrix, and f_e is the interaction force with the environment.

The leader device and the follower robot usually have different configurations in the teleoperation system. The robot controller designed in the Cartesian space will benefit teleoperation control and telepresence, by ignoring the different configurations of both the leader device and the following robot. In addition, the controller designed in the Cartesian space will also benefit the generalisation across different platforms with various configurations. Therefore, we derive the controller in the Cartesian space. Based on the kinematic equation of the manipulator, we describe the position, velocity and acceleration of the end-effector as,

$$x(t) = f(q) \tag{3}$$
$$\dot{x}(t) = J(q)\dot{q} \tag{4}$$
$$\ddot{x} = \dot{J}(q)\dot{q} + J(q)\ddot{q} \tag{5}$$

where the $\dot{x}$ and $\ddot{x}$ are the velocity and acceleration of the robot end-effector in Cartesian space. $\dot{J}(q)$ is the derivate of the Jacobian matrix.

Considering the Eqs. (1)-(5), we can attain the robot dynamics in Cartesian space,

$$\Lambda_p(q)\ddot{x} + B(q,\dot{q})\dot{x} + G_p(q) + T_f + D_u = T_c + F_e \tag{6}$$

where $\Lambda_p(q)$ is the inertia matrix, $B(q,\dot{q})$ is the Coriolis term, $G_p(q)$ is the gravity term in Cartesian space; T_f is the friction term and D_u is the modelling uncertainty.

$$G_p(q) = \bar{J}^T(q)G(q) \tag{7}$$
$$\Lambda_p(q) = (J(q)M^{-1}(q)J^T(q))^{-1} \tag{8}$$
$$B(q,\dot{q}) = \bar{J}(q)^T(C(q,\dot{q}) - M(q)\bar{J}(q)\dot{J}(q))\bar{J}(q) \tag{9}$$

$\bar{J}(q)$ is the dynamically consistent inverse of $J(q)$, which can be calculated as [11],

$$\bar{J} = M^{-1}(q)J_p^T(q)\Lambda_p(q) \tag{10}$$
$$T_f = \bar{J}^T(q)\tau_f \tag{11}$$
$$T_c = \bar{J}^T(q)\tau_c \tag{12}$$

We design the T_c,

$$T_c = \Lambda_p(q)\ddot{x} + B(q,\dot{q})\dot{x} + G_p(q) + T_f + D_u \tag{13}$$

where T_c is used to compensate for the dynamic force of the robot manipulator and track the desired pose.

Remark 1: Both T_f and D_u are relatively small, thus they are neglected in practice. To improve the control accuracy, neural network control techniques can be used to tackle the above torques.

B. Null-Space Control of Redundant Robot Manipulator

For the redundant manipulator, the null space can be used to achieve other purposes, such as obstacle avoidance, singularity avoidance, and orientation constraints, etc.

$$\tau_{cs} = H_p^T(q)\tau_{ns} \tag{14}$$

where $\tau_{cs} \in R^n$ is the control torque for the second tasks, and $H_p^T(q)$ represents the null space projector. Because the τ_{cs} only works in the null space, this control torque will not interface with the main control torque τ_c in Eq.(12). The τ_{ns} can be used for obstacle avoidance etc.

$$H_p^T(q) = [I - \bar{J}(q)J(q)]^T \tag{15}$$

$\bar{J}(q)$ is the dynamically consistent inverse of $J(q)$ in Eq.(10).

Remark 2: While the null space has various potential applications, we focus solely on optimising the joint angle near the middle of the working range to prevent any singularity issues during orientation tracking.

C. Compliant Interaction Control

The impedance control provides a way to achieve natural and compliant interactions between robots and their environment, which can be useful in a wide range of applications. The impedance control of 1-D model in Cartesian space can be represented as,

$$m_i\ddot{e}_i + d_i\dot{e}_i + k_i e_i = f_i \tag{16}$$

where the subscript i denote the ith dimension, m_i, d_i and k_i are the desired inertia, damping and stiffness, f_i is the interaction force. The impedance model is a mass-damping-spring system, which describes the relationship between the tracking errors and the contact force. To track the desired pose, we need to implement the translation impedance model and the orientation impedance model. The Eq.(16) directly describes the translation impedance model, however, the orientation tracking is complicated due to different representations. We adopt the quaternion-based orientation control for the teleoperation control, which is provided by the Franka Control Interface (FCI).

IV. Design and Evaluation Metrics of Teleoperation System

The developed system includes two teleoperation interfaces, a 3D mouse and a haptic device, as shown in 2. Ultrasound image feedback and RGB image feedback have been developed for the human operator. The human operator teleoperated the Franka robot arm, which was equipped with an ultrasound probe to scan on the ultrasound Phantom to acquire clear ultrasound images. Human operators will exert force f_h on the teleoperation interfaces. The contact force will be provided to the human operator by haptic feedback or monitor display.

A. Bilateral Teleoperation Control Design

In the bilateral teleoperation, the dynamics of the leader robot and follower robot in Cartesian space are given,

$$M_L(q_L)\ddot{x}_L + C_L(q_L, \dot{q}_L)\dot{x}_L + G_L(q_L) = u_L + f_h \quad (17)$$

$$M_F(q_F)\ddot{x}_F + C_F(q_F, \dot{q}_F)\dot{x}_F + G_F(q_F) = u_F + f_e \quad (18)$$

where $M_L(q_L)$ and $M_F(q_F)$ are the inertia matrix, $C_L(q_L, \dot{q}_L)$ and $C_F(q_F, \dot{q}_F)$ are the Coriolis and centrifugal terms, and $G_L(q_L)$ and $G_F(q_F)$ represent the gravity of the leader and follower robots[2] respectively. u_L and f_h are the control input and operator force for the leader robot. q_L and $\dot{q}_L$ are the joint position and velocity of leader robot. The $\dot{x}_L$ and $\ddot{x}_L$ are the velocity and acceleration of the leader robot in Cartesian space. u_F and f_e are the control input and interaction force of the follower robot. q_F and $\dot{q}_F$ are the joint position and velocity of the follower robot, the $\dot{x}_F$ and $\ddot{x}_F$ represent the velocity and acceleration of the follower robot in Cartesian space.

Impedance control models the relationship between the robot and the environment as a mass-spring-damper system. We designed the impedance controller in Cartesian space for the follower robot,

$$u_F = K_F(x_L - x_F) - D_F\dot{x}_F \quad (19)$$

where u_F is the control command of follower robot, K_F is the stiffness matrix, the D_F represents the damping matrix. x_L and x_F are the positions of the leader and follower robots, respectively.

The force feedback is designed to reflect the interaction force between the follower robot and its environment. The force feedback for the leader robot is designed as follows,

$$u_L = -K_L f_e - D_L\dot{x}_L \quad (20)$$

where u_L is the control input of the leader robot, D_L is the damping matrix. f_e is the interaction force between the follower robot and environment, K_L is the scaling parameter. To reflect the contact force on the haptic device side, we design the following controller,

$$f_m = -K_L f_e \quad (21)$$

where K_L is the scaling parameter to transform the contact force on the end-effector side to the haptic side. The maximum force feedback for the haptic device is usually small. For example, the maximum force of Touch X is 5N; therefore, we use the Eq.(21) to scale down the real contact force.

Remark 3: For the bilateral teleoperation by Touch X, as shown in Fig.3, force feedback is provided for the operator by Touch X, while the 3D mouse lacks force feedback. This difference in control systems is due to the presence or absence of force feedback. The control structure of the 3D mouse-based teleoperation system is shown in Fig. 5, in which a visual display, a monitor, reflexes the contact force.

[2]Note the leader robot refers to the teleoperation device, Touch X, and the follower robot refers to the Franka robot manipulator.

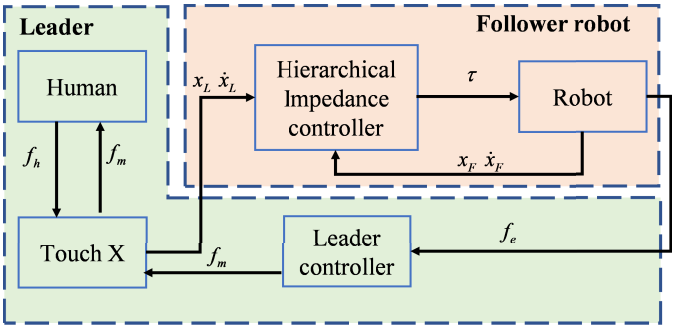

Fig. 3. The bilateral teleoperation control structure by haptic device, Touch X. The leader controller, Eq.(21) reflects the interaction force between the robot and the human body f_e to the handle of the haptic device f_m.

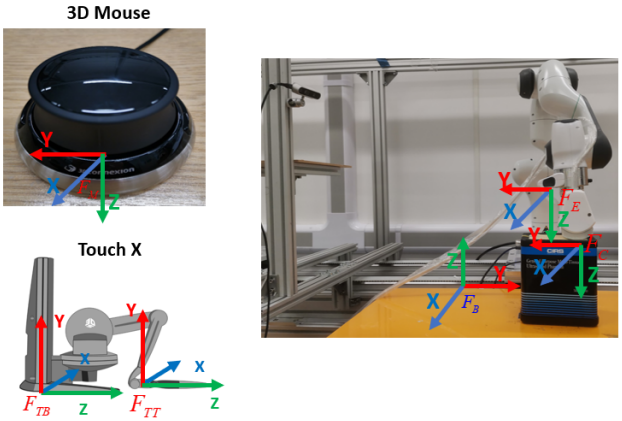

Fig. 4. The coordinate systems of two teleoperation interfaces.

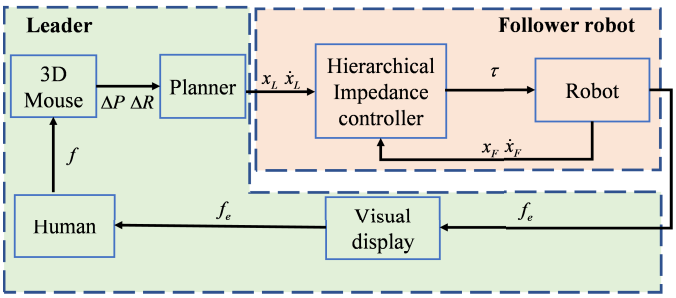

Fig. 5. The teleoperation control structure utilizes a 3D mouse, with a visual display employed to visualize the contact force (f_e) on the monitor.

B. The Coordinate Frames of the Teleoperation System

There are several coordinate systems in the robot-assisted ultrasound scanning system. We defined the coordinates used in this work: probe contact frame F_C, probe frame F_P, force sensor frame F_T, end-effector frame F_E, robot base frame F_B, touch tip frame F_{TT} and touch base frame F_{TB}, as shown in Fig. 4. Touch X was used as the leader device. A teleoperation control mapping algorithm was developed to map the relative pose between the Touch tip frame F_{TT} and the Touch base frame F_{TB} to the relative pose between robot base frame F_B and the end-effector frame F_E, in our previous work [34].

In this paper, ${}^{\varepsilon}T_{\varpi} \in SE(3)$ represents a homogeneous transformation matrix, ${}^{\varepsilon}R_{\varpi} \in SO(3)$ represents a rotation matrix, and ${}^{\varepsilon}P_{\varpi} \in R^3$ represents a translation vector.

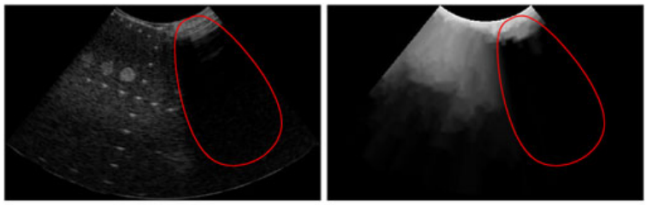

Fig. 6. (a) Ultrasound image. (b) Confidence map, adapted from [39]. Black block in the red circle, induced by an inappropriate orientation contact between the ultrasound probe and the Phantom.

ε represents the reference frame and ϖ denotes the goal frame. The pose of contact point between the probe and the Phantom can be described in robot base frame as,

$$^{B}T_{C} = {}^{B}T_{E}\,{}^{E}T_{C} \tag{22}$$

where ${}^{B}T_{E}$ is the transformation matrix from the robot base frame F_B to the end-effector F_E, and ${}^{E}T_{C}$ is the transformatation matrix from the end-effector frame F_E to the contact frame F_C. Before task execution, the transformation matrix used to obtain the relative pose between the end-effector and the probe's contact point is calibrated utilizing the dimensions of the fixture, which is used to fix the probe in the end-effector. The fixture is 3d printed, and the size and dimensions are known. Due to the contact force measured in the force sensor frame, we need to attain the force/ torque in the contact frame. Thus, we derive the transformation matrix from the contact frame to the force sensor frame,

$$^{C}T_{T} = {}^{C}T_{E}\,{}^{E}T_{T} \tag{23}$$

where ${}^{C}T_{T}$ is the transformation matrix from the probe contact frame F_C to the force sensor frame F_T, and ${}^{E}T_{T}$ is the transformatation matrix from the end-effector frame F_E to the force sensor frame F_T.

C. Ultrasound Image Quality Metrics

1) Confidence Map (CM): Ultrasound image quality is an important metric in assessing the effectiveness of teleoperation-based human-robot interfaces. However, the commonly used method of manual scoring by sonographers is time-consuming and expensive, particularly when dealing with a large number of images. The variation in ultrasound image quality is due to the effects of acoustic attenuation, absorption, and diffraction when ultrasound waves travel through biological tissues, leading to artefacts and shadows in the resulting images, as shown in Fig. 6.

Due to the specific process of ultrasound image (US) formation, the resulting images are not uniform in terms of quality. More precisely, ultrasound waves undergo acoustic attenuation, absorption and diffraction when traveling through biological tissues, as shown in Fig.6. The variation of image quality can be particularly important when an abrupt change in acoustic impedance occurs on the path of the wave [9]. A commonly observed artifact is shadowing, which corresponds to an important diminution of the amplitude of the ultrasound wave due to the presence of a strong attenuator. For the CM, we define the confidence map [9],

$$C : \Omega \rightarrow [0, 1] \tag{24}$$

where for a pixel $p \in \Omega$, $C(p)$ is a measure of the confidence in the image intensity $I(p)$.

Several automatic methods have been developed for assessing the quality of images [9]. One such method is the use of CM to evaluate image quality, and adjust the positioning of probes accordingly [39]. For instance, Chatelain et al. proposed a visual servoing technique that utilizes ultrasound CMs to optimize image quality [9]. More recently, Jiang et al. developed a vision-based ultrasound system that employs a confidence-based optimization algorithm to precisely reposition robotic ultrasound arms and avoid gaps between the probe and contact surface [7]. The confidence map approach has also been utilized to optimize the orientation of ultrasound probes for automatic normal positioning [6].

In this work, we require the ultrasound feature to lay in the centre of the image, one of the metric is the deviation angle between the centre of the feature and the centre of the image, as shown in Fig. 6.

2) Noisy: As previously noted, ultrasound (US) images are often plagued by high levels of noise stemming from the imaging process. However, this noise feature can be harnessed to assess the quality of US images. Specifically, the noise level in US images can be estimated by computing the mean and standard deviation of the difference between the original image and a filtered version of the same image. In our study, we employed the Wiener filter to eliminate noise from US images and calculate the corresponding noise feature [40],

$$\mu = \frac{\sum_{p_x \in \eta} \sum_{p_y \in \eta} I_x(p_x, p_y)}{P \times Q} \tag{25}$$

where $I_x(x, y)$ is the pixel intensity in pixel (x, y). μ is the average of pixel intensity in the US images, and σ represents the variance. $P \times Q$ represents the neighbour area around each pixel η.

$$\sigma^2 = \frac{\sum_{p_x \in \eta} \sum_{p_y \in \eta} I_x(p_x, p_y)^2}{P \times Q} - \mu^2 \tag{26}$$

where $I_x(p_x, p_y)$ is the pixel intensity. To improve the quality of the US, using the Wiener filter to remove the noise,

$$I_{k,f}(p_x, p_y) = \mu + \frac{\sigma^2 - v^2}{\sigma^2}(I_k(p_x, p_y) - \mu) \tag{27}$$

$$I_n = I_k - I_{k,f} \tag{28}$$

$$f_n = \bar{I}_n + \sigma_n \tag{29}$$

where f_n is the noise feature, $\bar{I}_n$ denotes the average noise and σ_n is the standard deviation.

D. Human Muscle Fatigue Metrics

Several Electromyography (EMG)-based teleoperation interfaces were presented [41], [42]. And the EMG could also be used to describe the stiffness of muscle, and the stiffness estimation was employed to variable stiffness controller of robot [43], [44]. The myoelectric activations of eight muscle

groups of the human hand and forearm were recorded using double differential electrodes. Various sEMG signal processing approaches were studied to evaluate the local muscle fatigue [38]. In this work, muscle fatigue refers to local muscle fatigue. On the other hand, Electromyography (EMG) signal has been used to estimate the fatigue of human arm [45]. The EMG arm band has eight channels to record the muscle contraction. Comparing the EMG signal for two different states of arm, when the arm is in the relaxing state, and the eight EMG signal is stable and low. The other one is the contact state, the eight EMG signal is high.

We utilise Median Frequency (MDF) and Root Mean-Square (RMS) to quantify the fatigue effects on frequency and amplitude, respectively. Firstly, the Amplitude analysis where RMS was used as a parameter for the temporal and amplitude changes in sEMG because of fatigue. Secondly, the spectral analysis where the fatigue parameter was MDF to detect the frequencies shift and spectral changes.

1) Time Domain Analysis: In this work, we adopt the time domain method [38] to calculate the volume of eight sEMG signal. Modulation of the amplitude due to muscular effort and/or fatigue represents the dominant change of sEMG signal in the time domain. First continuous EMG amplitude estimators consisted of full-wave rectifier followed by a resistorâcapacitor low-pass filter. In modern digital systems two indicators of sEMG amplitude are used: mean absolute value (MAV), also called average rectified value (ARV), and root-mean-square (RMS) value. They are defined by following equations,

$$MAV = \frac{1}{N}\sum_{i=1}^{N}|x_i| \tag{30}$$

$$RMS = \sqrt{\frac{1}{N}\sum_{i=1}^{N}x_i^2} \tag{31}$$

where x_i is the ith sample of a signal and N is the number of samples in the epoch.

2) Spectral Analysis: Similar to the temporal analysis, the sEMG of each channel was segmented into 1-seconds epochs. The spectrum for each epoch was computed using Short-time Fourier transform (STFT) to conform to the stationary requirement of the Fourier transform. In addition, a non-parametric approach was used since there are enough data and there was no underlying known structure within the signal.

MDF is defined as the frequency that divides the spectrum in two equal halves, where 50% of the total power within the epoch is reached. For each epoch, MDF was calculated according to the following equation:

$$\int_0^{MDF} P(f)df = \int_{MDF}^{f_s/2} P(f)df \tag{32}$$

where $P(f)$ is the PSD of the epoch and f_s is the sampling frequency. The MDF value for each epoch was fit to a first-degree polynomial equation to obtain its slope, denoted asΔMDF, which serves as an indicator of muscle fatigue [46]. We defined the EMG_p as the indiction of the muscle fatigue

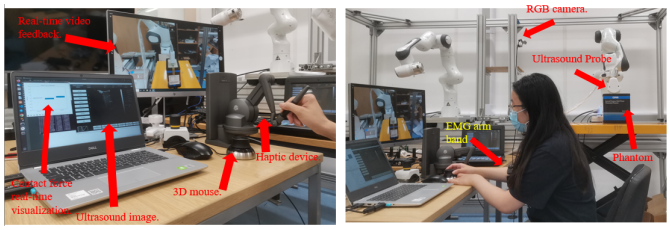

Fig. 7. The setup of the experimental platform. Two teleoperation interfaces, Touch X and 3D mouse, are used to teleoperate the robot arm to perform the medical examination.

in this work, which can be described as,

$$EMG\_p = \sum|\Delta RMS| + \sum|\Delta MDF| \tag{33}$$

where RMS was used as an indicator for this amplitude modulation, and the change of RMS values with time ΔRMS was a parameter for fatigue assessment [46].

V. Experimental Evaluation

The teleoperation system for ultrasound scanning includes teleoperation devices, a communication module, and a vision system, as shown in Fig. 7. On the human operator side, we developed two different teleoperation interfaces, a 3D mouse and a haptic device, Touch X. Human operators use the 3D mouse to teleoperate the position and orientation of the ultrasound probe without force feedback. To provide the force feedback, we use a bar graph with three bars to visualise the real-time contact force. These three bars in the bar graph represent X, Y and Z forces, respectively. We also visualise the real-time ultrasound images with a monitor. The RGB camera captures the remote scene of the robot side, and the real-time visual information is displayed on a different monitor.

The haptic device Touch X allows the human operator to control the motion and orientation of the probe, and the Touch X could also render the contact force between the probe and the Phantom. We used the EMG armband to monitor muscle contraction, and the signal of EMG is used to estimate the physical fatigue of human operators. A customised ultrasound machine, including the curved probe, was used to capture the ultrasound images. A 3D printing component was used to connect the probe with the end-effector of the robot manipulator. A video card was used to convert the real-time ultrasound video to the laptop. The robot operating system (ROS Melodic) was used to communicate with different modules: the robot control system, vision system, and ultrasound image system.

A 7-DoF Franka Emika Panda equipped with an ultrasound probe to perform the scanning task. A Touch X was used as the teleoperation device. A realsense camera (D435i) was used to record RGB images, which could also provide visual feedback during human teleoperation. Control computer running Ubuntu 18.04, which was connected to the Touch X device, Franka Emika Panda, and the camera. ROS was used to integrate different components. The whole experimental procedure was conducted in accordance with the Faculty Research Ethics Committee, and the protocol was approved by the UWE Research Ethics Committee (UWE REC REF No: FET-2122-59).

TABLE II
PARAMETERS OF THE IMPEDANCE CONTROLLER

End-effector	Stiffness matrix		Damping matrix	
Position	$K_p = \begin{bmatrix} 200 & 0 & 0 \\ 0 & 200 & 0 \\ 0 & 0 & 50 \end{bmatrix}$		$D_p = \begin{bmatrix} 30 & 0 & 0 \\ 0 & 30 & 0 \\ 0 & 0 & 15 \end{bmatrix}$	
Orientation	$K_O = \begin{bmatrix} 50 & 0 & 0 \\ 0 & 50 & 0 \\ 0 & 0 & 50 \end{bmatrix}$		$D_O = \begin{bmatrix} 15 & 0 & 0 \\ 0 & 15 & 0 \\ 0 & 0 & 15 \end{bmatrix}$	

Table II outlines the parameters of the teleoperation system. In the case of the orientation impedance controller, the quaternion representation is utilized.

A. Medical Examination Scanning Task Description

To evaluate the performance of the designed two interfaces, we conduct robot-assisted sonography on Phantom. The Phantom is a standard medical examination tool for sonographers' training and examination. The participants need to control the robot equipped with the ultrasound probe to approach the Phantom and scan the Phantom with appropriate contract force to acquire high-quality ultrasound images by adjusting the motion and orientation simultaneously.

After participants have completed the task, participants will be asked to complete the NASA-TLX questionnaire [47]. The NASA-TLX questionnaire assesses workload for both interfaces by giving scores in six areas: Mental Demand (MD), Physical Demand (PD), Temporal Demand (TD), Performance (PE), Effort (EF) and Frustration (FR). All six aspects were divided into 0-21, with higher scores indicating higher levels of participant satisfaction. Additionally, the data during the completion of the experiment is recorded and evaluated at the end. The NASA-TLX questionnaire focuses on assessing the subjective experience of the participants, while the collected data during the completion is more focused on the objective performance of the task, such as accuracy, stability, and duration of the task.

B. The Tracking Performance of the Bilateral Teleoperation System

The position tracking in the X-Y-Z direction of the teleoperation by Touch X is shown in Fig.8. The follower robot effectively tracks the leader robot's desired position. Figure 9 displays the quaternion-based orientation tracking of the teleoperation system. However, the impedance controller with small stiffness introduces tracking errors and delays in both position and orientation. This is an inherent limitation of the compliant controller. While the small stiffness provides better compliant performance when interacting with humans, the low stiffness results in reduced tracking accuracy. Fig. 10 displays the 3D trajectory, which highlights the tracking error caused by the low-impedance controller.

C. The Learning and Task Execution Time

We chose the learning time and task execution time as the evaluation metrics. The learning time can describe the intuitives of the teleoperation interface. The task execution time could represent work efficiency. The performance of the efficiency of different teleoperation interfaces is an important aspect. These objective metrics can be used to describe the performance of the different teleoperation interfaces. As shown

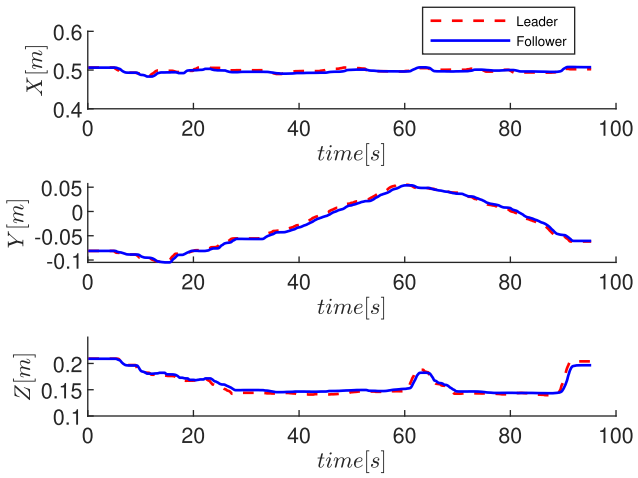

Fig. 8. Position tracking in X-Y-Z directions via Touch X teleoperation.

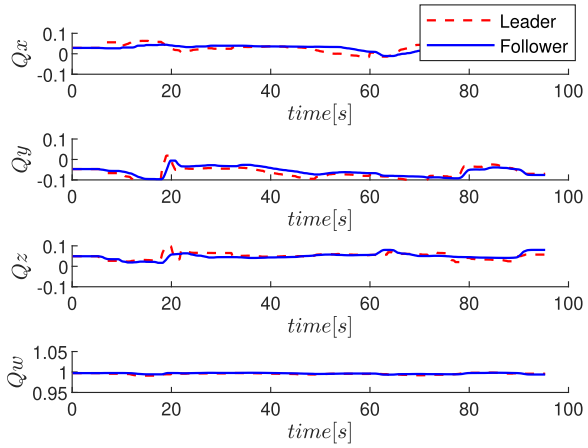

Fig. 9. Quaternion-based orientation tracking via Touch X teleoperation.

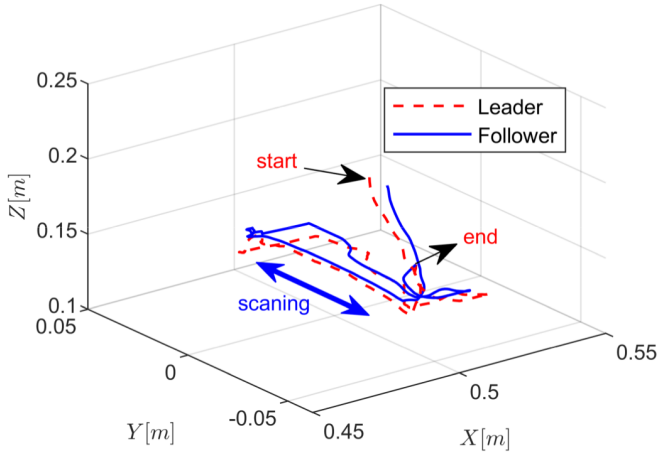

Fig. 10. Trajectory tracking in 3D dimension in tele-sonography by Touch X.

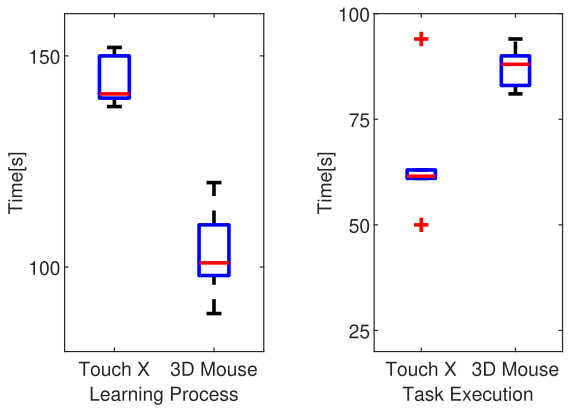

Fig. 11. Comparison of learning and performing time for two teleoperation interfaces. The learning process refers to the time taken in the training phase prior to the user study experiment, while task execution refers to the time taken to perform the task.

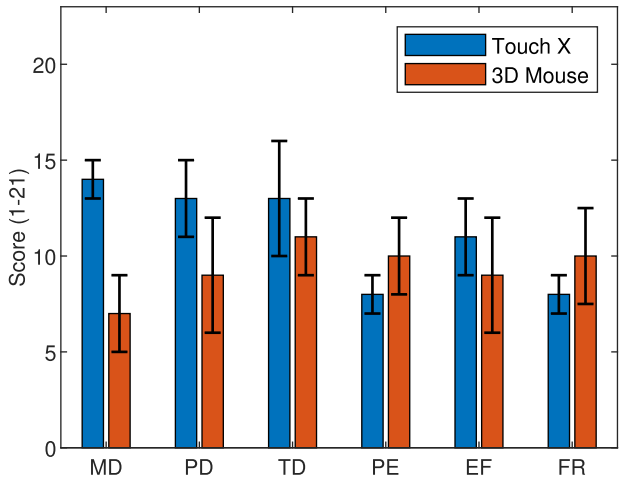

Fig. 12. User feedback evaluation based on NASA-TLX scores for two different human-robot interfaces.

TABLE III
QUANTITATIVE AND OBJECTIVE PERFORMANCE EVALUATION ON PHANTOM

	Force error (N)	Time mean (s)	Orientation error	Noise	Muscle fatigue (EMG)
3D Mouse	7.4	84	8	18.4	76.23
Touch X	3.8	61	5.4	14.3	89.34

in Fig. 11, the learning time of Touch X is larger than the 3D mouse, which means that the 3D mouse is easy to learn. However, the execution time by Touch X is shorter than the 3D mouse.

D. Performance Evaluation Based on NASA-TLX

In the experiment, participants were asked to complete the same task using Touch X and 3D Mouse, after which they completed the NASA-TLX questionnaire to give scores in six aspects: MD, PD, TD, PE, EF and FR. The scores are presented in Fig. 12 as a box plot, to graphically demonstrate the maximum, minimum value (shown as horizontal lines from top to bottom respectively) as well as mean value (shown as a cross point). In general, 3D Mouse users gave lower scores in more aspects, including MD, PD, TD and EF. The difference in scores can be spotted most evidently in MD, where the mean value of Touch X (13.4) is almost twice as high as that of 3D Mouse (6.8). The distinction between Touch X and 3D Mouse in PD and EF are also noticeable, with a difference of 4.2 and 4, correspondingly. On the contrary, participants with Touch X had shown lower scores in PE and FR, indicating that despite the higher demand and effort of the task, the performance was slightly better with lower frustration using Touch X.

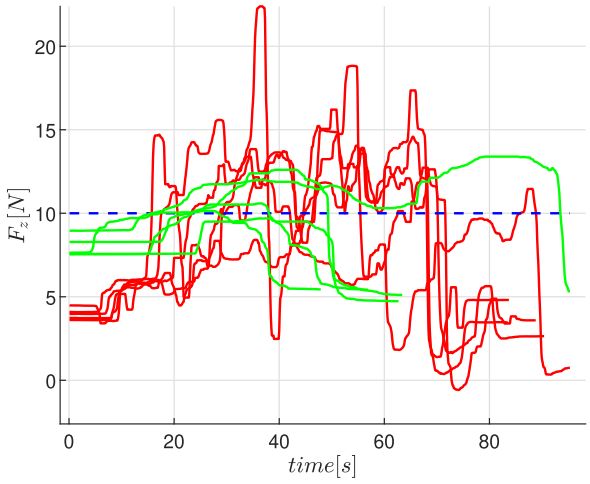

Fig. 13. Comparison of contact force between haptic and 3D mouse teleoperation interfaces across five experiments during scanning. The red lines represent the contact force by the 3D mouse, while the green lines represent the contact force by the Touch X interface. The blue line represents the desired contact force.

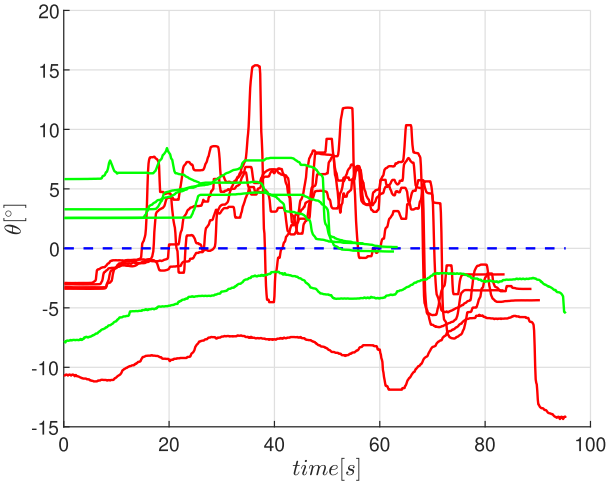

Fig. 14. Deviation angle of the centre of the confidence map images acquired by the two different interfaces across five experiments during scanning. The red lines represent the deviation angle by the 3D mouse, while the green lines represent the deviation angle by the Touch X interface. The blue line represents the ideal orientation with zero deviation.

E. Contact Force and Image Quality

The contact force during teleoperation scanning via the Touch X and 3D Mouse interfaces is depicted in Fig. 13. The desired contact force was set to 10N before the experiment. The results indicate that the variance of the contact force by Touch X is lower than that by the 3D Mouse. In addition, the deviation angle of the confidence map images' center acquired by the 3D Mouse is larger than that of the Touch X, as illustrated in Fig 14. Despite this, the Touch X is more flexible to operate than the 3D Mouse, and it provides better work efficiency. A comparison of muscle fatigue and image noise is presented in Table. III. While the Touch X outperforms the 3D Mouse regarding image quality, it requires more effort and can cause muscle fatigue.

VI. Conclusion

This paper presented the development and evaluation of two different interfaces for robot-assisted ultrasound scanning through a user experience study. The two teleoperation interfaces include a 3D mouse and a haptic device, Touch X, each with corresponding teleoperation control algorithms. Comprehensive metrics were proposed to evaluate the performance of different teleoperation interfaces during ultrasound scanning tasks, including the quality of the acquired ultrasound image and robot state data. Based on these metrics, the performance of Touch X was found to be better than that of the 3D mouse, except for the aspect of muscle fatigue. Our future work will investigate machine learning techniques and shared control to improve the teleoperation system's autonomy, reducing human operators' mental and physical workload.

Acknowledgment

The authors would like to express their gratitude to Rebecca Harris and Nicola Papastavrou Brooks from University Hospitals Bristol and Weston for providing the Phantom and valuable training on ultrasound scanning.

References

[1] Q. Huang, J. Zhou, and Z. Li, "Review of robot-assisted medical ultrasound imaging systems: Technology and clinical applications," *Neurocomputing*, vol. 559, Nov. 2023, Art. no. 126790.

[2] Z. Jiang, S. E. Salcudean, and N. Navab, "Robotic ultrasound imaging: State-of-the-art and future perspectives," *Med. Image Anal.*, vol. 89, Oct. 2023, Art. no. 102878.

[3] F. Conti, J. Park, and O. Khatib, "Interface design and control strategies for a robot assisted ultrasonic examination system," in *Proc. 12th Int. Symp. Exp. Robot.* Cham, Switzerland. Berlin, Germany: Springer, Aug. 2014, pp. 97–113.

[4] Y. Huang, W. Xiao, C. Wang, H. Liu, R. Huang, and Z. Sun, "Towards fully autonomous ultrasound scanning robot with imitation learning based on clinical protocols," *IEEE Robot. Autom. Lett.*, vol. 6, no. 2, pp. 3671–3678, Apr. 2021.

[5] X. Ma, Z. Zhang, and H. K. Zhang, "Autonomous scanning target localization for robotic lung ultrasound imaging," in *Proc. IEEE/RSJ Int. Conf. Intell. Robots Syst. (IROS)*, Sep. 2021, pp. 9467–9474.

[6] Z. Jiang et al., "Automatic normal positioning of robotic ultrasound probe based only on confidence map optimization and force measurement," *IEEE Robot. Autom. Lett.*, vol. 5, no. 2, pp. 1342–1349, Apr. 2020.

[7] Z. Jiang et al., "Precise repositioning of robotic ultrasound: Improving registration-based motion compensation using ultrasound confidence optimization," *IEEE Trans. Instrum. Meas.*, vol. 71, pp. 1–11, 2022.

[8] Q. Huang, J. Lan, and X. Li, "Robotic arm based automatic ultrasound scanning for three-dimensional imaging," *IEEE Trans. Ind. Informat.*, vol. 15, no. 2, pp. 1173–1182, Feb. 2019.

[9] P. Chatelain, A. Krupa, and N. Navab, "Confidence-driven control of an ultrasound probe," *IEEE Trans. Robot.*, vol. 33, no. 6, pp. 1410–1424, Dec. 2017.

[10] J. Zhang et al., "Self-adaptive ultrasound scanning system for imaging human spine," *IEEE Trans. Ind. Electron.*, vol. 69, no. 1, pp. 570–581, Jan. 2022.

[11] L. Santos and R. Cortesão, "Computed-torque control for robotic-assisted tele-echography based on perceived stiffness estimation," *IEEE Trans. Autom. Sci. Eng.*, vol. 15, no. 3, pp. 1337–1354, Jul. 2018.

[12] M. C. Roshan, A. Pranata, and M. Isaksson, "Robotic ultrasonography for autonomous non-invasive diagnosis—A systematic literature review," *IEEE Trans. Med. Robot. Bionics*, vol. 4, no. 4, pp. 863–874, Nov. 2022.

[13] F. von Haxthausen, S. Böttger, D. Wulff, J. Hagenah, V. García-Vázquez, and S. Ipsen, "Medical robotics for ultrasound imaging: Current systems and future trends," *Current Robot. Rep.*, vol. 2, no. 1, pp. 55–71, Mar. 2021.

[14] I. Ozdamar, M. Laghi, G. Grioli, A. Ajoudani, M. G. Catalano, and A. Bicchi, "A shared autonomy reconfigurable control framework for telemanipulation of multi-arm systems," *IEEE Robot. Autom. Lett.*, vol. 7, no. 4, pp. 9937–9944, Oct. 2022.

[15] L. Hindemith, O. Bruns, A. M. Noller, N. Hemion, S. Schneider, and A.-L. Vollmer, "Interactive robot task learning: Human teaching proficiency with different feedback approaches," *IEEE Trans. Cognit. Develop. Syst.*, vol. 15, no. 4, pp. 1938–1947, Dec. 2023.

[16] N. Wang, C. Chen, and A. D. Nuovo, "A framework of hybrid force/motion skills learning for robots," *IEEE Trans. Cognit. Develop. Syst.*, vol. 13, no. 1, pp. 162–170, Mar. 2021.

[17] H. Qiao, Y.-X. Wu, S.-L. Zhong, P.-J. Yin, and J.-H. Chen, "Brain-inspired intelligent robotics: Theoretical analysis and systematic application," *Mach. Intell. Res.*, vol. 20, no. 1, pp. 1–18, Feb. 2023.

[18] H. Qiao, S. Zhong, Z. Chen, and H. Wang, "Improving performance of robots using human-inspired approaches: A survey," *Sci. China Inf. Sci.*, vol. 65, no. 12, pp. 1–31, Dec. 2022.

[19] P. Shi, W. Sun, X. Yang, I. J. Rudas, and H. Gao, "Master-slave synchronous control of dual-drive gantry stage with cogging force compensation," *IEEE Trans. Syst. Man, Cybern. Syst.*, vol. 53, no. 1, pp. 216–225, Jan. 2023.

[20] Z. Liu, W. Lin, X. Yu, J. J. Rodríguez-Andina, and H. Gao, "Approximation-free robust synchronization control for dual-linear-motors-driven systems with uncertainties and disturbances," *IEEE Trans. Ind. Electron.*, vol. 69, no. 10, pp. 10500–10509, Oct. 2022.

[21] Z. Li, X. Yu, J. Qiu, and H. Gao, "Cell division genetic algorithm for component allocation optimization in multifunctional placers," *IEEE Trans. Ind. Informat.*, vol. 18, no. 1, pp. 559–570, Jan. 2022.

[22] H. Gao, Z. Li, X. Yu, and J. Qiu, "Hierarchical multiobjective heuristic for PCB assembly optimization in a beam-head surface mounter," *IEEE Trans. Cybern.*, vol. 52, no. 7, pp. 6911–6924, Jul. 2022.

[23] Y. Fu, W. Lin, X. Yu, J. J. Rodríguez-Andina, and H. Gao, "Robot-assisted teleoperation ultrasound system based on fusion of augmented reality and predictive force," *IEEE Trans. Ind. Electron.*, vol. 70, no. 7, pp. 7449–7456, Jul. 2023.

[24] Y. Wu, P. Balatti, M. Lorenzini, F. Zhao, W. Kim, and A. Ajoudani, "A teleoperation interface for loco-manipulation control of mobile collaborative robotic assistant," *IEEE Robot. Autom. Lett.*, vol. 4, no. 4, pp. 3593–3600, Oct. 2019.

[25] A. Naceri et al., "Tactile robotic telemedicine for safe remote diagnostics in times of corona: System design, feasibility and usability study," *IEEE Robot. Autom. Lett.*, vol. 7, no. 4, pp. 10296–10303, Oct. 2022.

[26] D. Raina et al., "Comprehensive telerobotic ultrasound system for abdominal imaging: Development and in-vivo feasibility study," in *Proc. Int. Symp. Med. Robot. (ISMR)*, Nov. 2021, pp. 1–7.

[27] M. Aggravi, D. A. L. Estima, A. Krupa, S. Misra, and C. Pacchierotti, "Haptic teleoperation of flexible needles combining 3D ultrasound guidance and needle tip force feedback," *IEEE Robot. Autom. Lett.*, vol. 6, no. 3, pp. 4859–4866, Jul. 2021.

[28] N. Enayati, G. Ferrigno, and E. De Momi, "Skill-based human–robot cooperation in tele-operated path tracking," *Auto. Robots*, vol. 42, no. 5, pp. 997–1009, Jun. 2018.

[29] S. Gholami, M. Lorenzini, E. De Momi, and A. Ajoudani, "Quantitative physical ergonomics assessment of teleoperation interfaces," *IEEE Trans. Hum.-Mach. Syst.*, vol. 52, no. 2, pp. 169–180, Apr. 2022.

[30] G. Doisy, J. Meyer, and Y. Edan, "The impact of human–Robot interface design on the use of a learning robot system," *IEEE Trans. Hum.-Mach. Syst.*, vol. 44, no. 6, pp. 788–795, Dec. 2014.

[31] P. Abolmaesumi, S. E. Salcudean, W. H. Zhu, S. P. DiMaio, and M. R. Sirouspour, "A user interface for robot-assisted diagnostic ultrasound," in *Proc. IEEE Int. Conf. Robot. Autom. (ICRA)*, May 2001, pp. 1549–1554.

[32] C. Pacchierotti, M. Abayazid, S. Misra, and D. Prattichizzo, "Teleoperation of steerable flexible needles by combining kinesthetic and vibratory feedback," *IEEE Trans. Haptics*, vol. 7, no. 4, pp. 551–556, Oct. 2014.

[33] D. Black, Y. Oloumi Yazdi, A. H. Hadi Hosseinabadi, and S. Salcudean, "Human teleoperation—A haptically enabled mixed reality system for teleultrasound," *Hum.–Comput. Interact.*, pp. 1–24, Jun. 2023, doi: 10.1080/07370024.2023.2218355.

[34] G. Zhao, C. Zeng, W. Si, and C. Yang, "A human-robot collaboration method for uncertain surface scanning," *CAAI Trans. Intell. Technol.*, pp. 1–12, May 2023, doi: 10.1049/cit2.12227.

[35] Q. Huang and J. Lan, "Remote control of a robotic prosthesis arm with six-degree-of-freedom for ultrasonic scanning and three-dimensional imaging," *Biomed. Signal Process. Control*, vol. 54, Sep. 2019, Art. no. 101606.

[36] C. Yang, M. Jiang, M. Chen, M. Fu, J. Li, and Q. Huang, "Automatic 3-D imaging and measurement of human spines with a robotic ultrasound system," *IEEE Trans. Instrum. Meas.*, vol. 70, pp. 1–13, 2021.

[37] Q. Huang et al., "Anatomical prior based vertebra modelling for reappearance of human spines," *Neurocomputing*, vol. 500, pp. 750–760, Aug. 2022.

[38] M. Cifrek, V. Medved, S. Tonković, and S. Ostojić, "Surface EMG based muscle fatigue evaluation in biomechanics," *Clin. Biomech.*, vol. 24, no. 4, pp. 327–340, May 2009.

[39] A. Karamalis, W. Wein, T. Klein, and N. Navab, "Ultrasound confidence maps using random walks," *Med. Image Anal.*, vol. 16, no. 6, pp. 1101–1112, Aug. 2012.

[40] M. Akbari et al., "Robotic ultrasound scanning with real-time image-based force adjustment: Quick response for enabling physical distancing during the COVID-19 pandemic," *Frontiers Robot. AI*, vol. 8, Mar. 2021, Art. no. 645424.

[41] A. Dwivedi, D. Shieff, A. Turner, G. Gorjup, Y. Kwon, and M. Liarokapis, "A shared control framework for robotic telemanipulation combining electromyography based motion estimation and compliance control," in *Proc. IEEE Int. Conf. Robot. Autom. (ICRA)*, May 2021, pp. 9467–9473.

[42] J. Luo, Z. Lin, Y. Li, and C. Yang, "A teleoperation framework for mobile robots based on shared control," *IEEE Robot. Autom. Lett.*, vol. 5, no. 2, pp. 377–384, Apr. 2020.

[43] C. Zeng, C. Yang, H. Cheng, Y. Li, and S.-L. Dai, "Simultaneously encoding movement and sEMG-based stiffness for robotic skill learning," *IEEE Trans. Ind. Informat.*, vol. 17, no. 2, pp. 1244–1252, Feb. 2021.

[44] C. Yang, C. Zeng, P. Liang, Z. Li, R. Li, and C.-Y. Su, "Interface design of a physical human–Robot interaction system for human impedance adaptive skill transfer," *IEEE Trans. Autom. Sci. Eng.*, vol. 15, no. 1, pp. 329–340, Jan. 2018.

[45] T.-C. Lin, A. U. Krishnan, and Z. Li, "Physical fatigue analysis of assistive robot teleoperation via whole-body motion mapping," in *Proc. IEEE/RSJ Int. Conf. Intell. Robots Syst. (IROS)*, Nov. 2019, pp. 2240–2245.

[46] A. Ebied, A. M. Awadallah, M. A. Abbass, and Y. El-Sharkawy, "Upper limb muscle fatigue analysis using multi-channel surface EMG," in *Proc. 2nd Novel Intell. Lead. Emerg. Sci. Conf. (NILES)*, Oct. 2020, pp. 423–427.

[47] S. G. Hart and L. E. Staveland, "Development of NASA-TLX (Task load index): Results of empirical and theoretical research," *Adv. Psychol.*, vol. 52, pp. 139–183, Jan. 1988.

Weiyong Si (Member, IEEE) received the M.S. degree in aerospace engineering from the Beijing Institute of Technology, China, in 2018, and the Ph.D. degree in robotics from the University of the West of England, Bristol, U.K., in 2023. He is currently a Lecturer with the Robotics and Embedded Intelligent Systems Laboratory, University of Essex, Colchester, U.K. His research interests include robot learning, robot-assisted medical examination, teleoperation, and robot control.

Ning Wang (Member, IEEE) received the M.Phil. and Ph.D. degrees in electronics engineering from the Department of Electronics Engineering, The Chinese University of Hong Kong, Hong Kong, in 2007 and 2011, respectively. She is currently a Senior Lecturer of robotics with the Bristol Robotics Laboratory, University of the West of England, U.K. Her research interests include signal processing, intelligent data analysis, human–robot interaction, and autonomous driving.

Chenguang Yang (Fellow, IEEE) received the B.Eng. degree in measurement and control from Northwestern Polytechnical University, Xi'an, China, in 2005, and the Ph.D. degree in control engineering from the National University of Singapore, Singapore, in 2010.

From 2009 to 2010, he was a Post-Doctoral Trainee in human robotics at Imperial College London, London, U.K. His research interests include human–robot interaction and intelligent system design.

Dr. Yang was a recipient of the U.K. EPSRC UKRI Innovation Fellowship, the EU Marie Curie International Incoming Fellowship, IEEE TRANSACTIONS ON ROBOTICS Best Paper Award in 2012, and IEEE TRANSACTIONS ON NEURAL NETWORKS AND LEARNING SYSTEMS Outstanding Paper Award in 2022. He is the Corresponding Co-Chair of the IEEE Technical Committee on Collaborative Automation for Flexible Manufacturing.